Abbreviations

EID = energy-integrating detector, NPS = noise power spectrum, PCD = photon-counting detector, TNC = true noncontrast, TTF = task transfer function, VNC = virtual noncontrast

Summary

Virtual noncontrast images from contrast-enhanced arterial and venous phase abdominal scans acquired using photon-counting detector CT yielded accurate attenuation values and good overall image quality.

Key Results

- In this retrospective study of 100 consecutive adults, virtual noncontrast (VNC) abdominal images acquired with photon-counting detector CT resulted in accurate attenuation compared with true noncontrast (TNC) images (mean absolute attenuation errors less than 5 HU in 76% and less than 10 HU in 95% of measurements).
- Subjective image quality was rated lower in VNC images for all criteria (for all, $P < .001$); however, diagnostic quality, defined as an image quality score greater than or equal to 3, was reached in 99%–100% of patients.
- In a phantom, VNC images exhibited 33% higher image noise and blotchier noise texture (average spatial frequency of 0.2 mm^{-1} vs 0.14 mm^{-1}) but similar spatial resolution compared with TNC images.

Materials and Methods

Patients

This single-center retrospective study was conducted at an academic medical center and received institutional review board and local ethics committee approval. All patients in the study provided written informed consent.

Consecutive patients who underwent a follow-up thoracoabdominal CT examination for aortic abnormalities that included TNC and contrast-enhanced arterial and portal venous scans from July 2021 to October 2021 were retrospectively searched. Inclusion criteria were age 18 years or older and imaging performed with a first-generation dual-source PCD CT scanner (NAEOTOM Alpha, version syngo CT VA40; Siemens Healthcare). Exclusion criteria were examinations performed with high-pitch arterial phase CT (pitch factor >3) and those performed with an EID CT scanner.

CT Scan Protocol

In the patients and phantom, imaging was performed with a first-generation, dual-source PCD CT scanner equipped with two cadmium telluride PCDs. All scans were acquired in the single-source, multienergy mode (QuantumPlus) with a tube voltage of 120 kV, collimation of 144 × 0.4 mm, spiral pitch factor of 1.2, and gantry rotation time of 0.25 second.

In the patients, the imaging protocol included TNC and contrast-enhanced arterial and portal venous thoracoabdominal scans. As recommended by the manufacturer, the tube current–time product was set to an image quality level of 68, using automated tube current modulation (CARE Dose4D, Siemens Healthcare). The tube current was further adapted depending on the imaging task (CARE kV; Siemens Healthcare); it was optimized for noncontrast during the TNC scan, for vascular structures during the contrast-enhanced arterial scan, and for soft tissue with contrast media during the portal venous scan.

The contrast-enhanced scans were acquired after the injection of 70 mL of contrast material (370 mg iodine per mL, iopromide [Ultravist; Bayer Healthcare]), starting with a 40-mL bolus of iodinated contrast material followed by a 60-mL 1:1 mixture of contrast material and saline solution, and completed with a saline chaser of 30 mL. The flow rate was 4 mL/sec. Bolus tracking in the ascending aorta with a threshold of 140 HU at 90 kV and a delay of 12 seconds was used to initiate arterial scanning. The portal venous scan was acquired 70 seconds after contrast material injection.

Image Reconstruction

In the patients and phantom, all images were reconstructed in the axial plane with a soft-tissue reconstruction kernel (Br36) using quantum iterative reconstruction at the highest strength level of 4. The section thickness was 2 mm and the increment was 1.6 mm. VNC images were reconstructed from the arterial and portal venous phases in the patients (Fig 1).

Assessment of Objective Image Quality

Patients.—Two readers (V.M., in training with 2 years of experience in abdominal imaging, and S.B., a medical student) independently measured the CT attenuation on TNC and VNC images reconstructed from arterial and portal venous phase CT by placing regions of interest in the following areas: aorta (at the level of the origin of the superior mesentery artery), right and left liver lobes, spleen, kidney, urinary bladder, and paravertebral muscle. Both readers participated in a supervised training session with an experienced, board-certified radiologist (A.E., a board-certified radiologist with 9 years of experience in abdominal imaging) during which 10 patients were measured. The region of interest was initially placed in the portal venous reconstruction, carefully avoiding adjacent structures, and was then copied to the TNC and VNC images reconstructed from arterial and portal venous phase CT. All three image sets were linked to show identical anatomic structures when scrolling. Interscan position differences due to breathing and patient movement were manually adjusted. The region of interest diameter was chosen as large as possible, ranging from 10 mm to 40 mm (Fig 2).

The accuracy of the attenuation on VNC images was assessed by calculating the absolute error of attenuation (VNC_{error}) as compared with TNC images as follows:

$$VNC_{error} = \left| HU_{VNC} - HU_{TNC} \right|.$$

HU_{VNC} refers to the attenuation on VNC reconstructions and HU_{TNC} to the attenuation on TNC images.

In addition, all CT studies were reviewed for hypoattenuating hepatic lesions with at least an 8-mm diameter by one reader (V.M.). To determine lesion-to-background contrast, CT attenuation was measured in these lesions and the adjacent liver parenchyma.

Phantom.—The aim of this part of the study was to compare image noise, spatial resolution, and objective image quality between VNC and TNC images. Therefore, image noise magni-

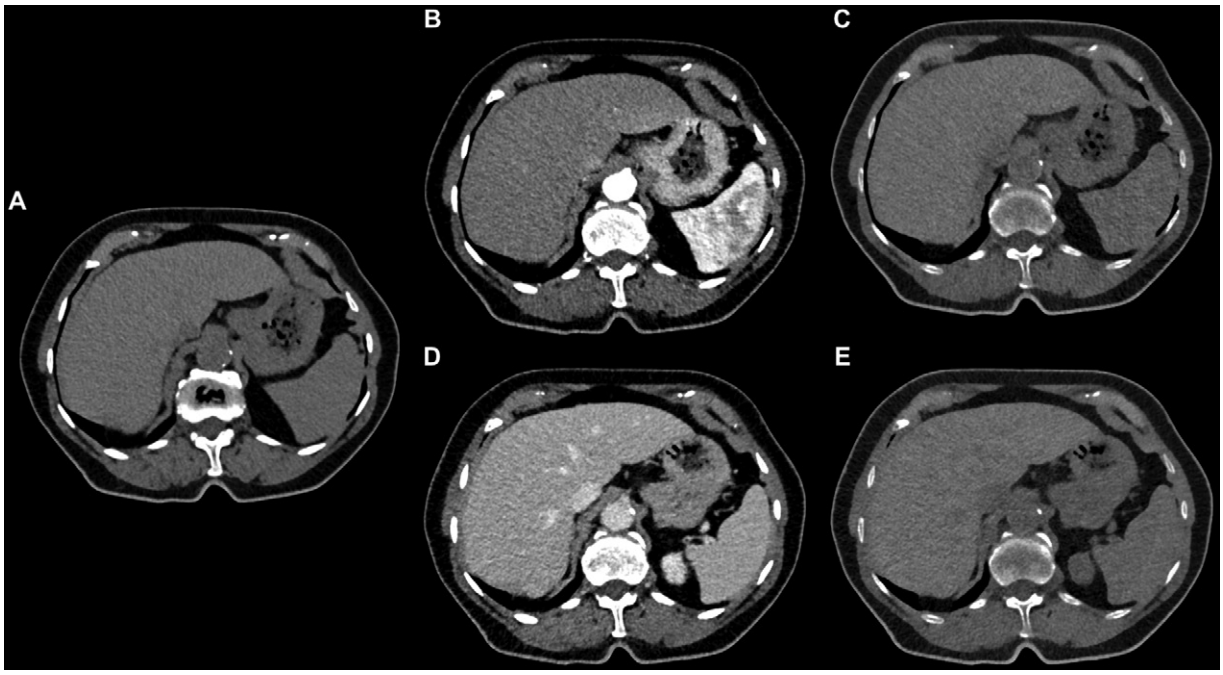

Figure 1: Representative CT images obtained in an 84-year-old woman referred for follow-up examination after endovascular aortic repair. Axial CT images acquired with thoracoabdominal photon-counting detector CT show **(A)** true noncontrast (TNC), **(B)** contrast-enhanced arterial, **(C)** arterial virtual noncontrast (VNC), **(D)** portal venous, and **(E)** venous VNC images. Slight differences in image noise texture can be depicted when comparing VNC (**C, E**) with TNC (**A**).

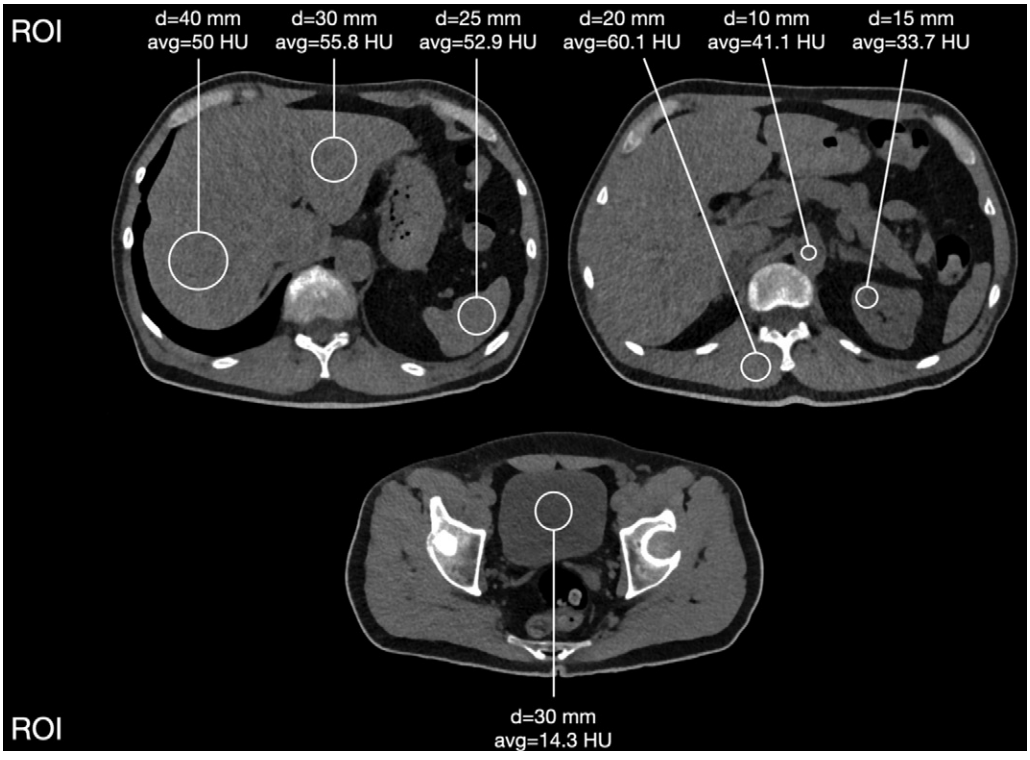

Figure 2: CT attenuation measurements in a 58-year-old man referred for follow-up examination after an acute type B aortic dissection. Axial CT images acquired with photon-counting detector CT depict exemplary region of interest (ROI) measurements on venous virtual noncontrast reconstructions. avg = average attenuation within region of interest, d = diameter of region of interest.

tude and texture were assessed using the noise power spectrum (NPS); spatial resolution was assessed using the task transfer function (TTF); and overall image quality was assessed using the detectability index. A 25-cm-diameter cylindrical, water-filled phantom with three central cylindrical inserts (each 10 cm in diameter) and a homogeneous area was imaged with the same

PCD CT scanner (27). Identical scan and reconstruction parameters were used as in patients. The volume CT dose index of the phantom scan was 2.4 mGy. All scans were repeated three times within a minute.

In short, the homogeneous area was used to measure the NPS and the low-contrast insert with polyethylene (CT attenuation difference to background at 120 kV of 80 HU), representing a contrast difference in abdominal imaging, to determine the TTF. The detectability index was calculated as a surrogate to estimate objective image quality and included the lesion-to-background ratio determined from hepatic lesions found in patients (28). A detectability index value greater than or equal to 5 has been described as indicating high diagnostic accuracy (27). A detailed description of the methodology can be found in Appendix E1 (online).

Assessment of Subjective Image Quality

Subjective image quality of TNC and VNC images in the patients was assessed in randomized order by two readers independently (A.E., a board-certified radiologist with 9 years of experience in abdominal imaging, and K.M., a board-certified radiologist with 8 years of experience in abdominal imaging). Both readers were blinded to the image reconstructions.

Image noise, delineation of small structures, and overall image quality were assessed using a five-point discrete visual scale adapted from a previous publication (29), whereby 5 is excellent, 4 is good, 3 is moderate, 2 is poor, and 1 is nondiagnostic. Delineation of small structures was evaluated based on the conspicuity of small blood vessels, adrenal glands, and small lymph nodes (29). Noise texture was evaluated using a five-point discrete visual scale such that 5 indicates no pixilation or blotchy appearance, 4 indicates minor pixilation or blotchy appearance not affecting diagnostic confidence, 3 indicates moderate pixilation or blotchy appearance mildly limiting diagnostic confidence, 2 indicates elevated pixilation or blotchy appearance reducing diagnostic confidence, and 1 indicates major pixilation or blotchy appearance with poor diagnostic confidence. All images were assessed for artifacts (ie, ring or streak artifacts and areas of residual contrast enhancement) by one reader (A.E.). Furthermore, the percentage of ratings deemed diagnostic, defined as an overall image quality score greater than or equal to 3, was determined for all three reconstructions.

Statistical Analysis

Quantitative variables with normal distribution are expressed as means ± SDs, while nonnormally distributed variables are presented as medians and IQRs. Categorical variables are presented as counts and percentages. Interreader agreement was quantified with the Krippendorff α coefficient (0 = no agreement, 1 = perfect agreement). For further calculation, mean attenuation values were computed based on the measurements of both readers and corresponding absolute attenuation errors of VNC images were calculated. The paired *t* test with Bonferroni correction was applied to compare the absolute attenuation errors of VNC images reconstructed from arterial and venous phase CT. The Friedman test with post hoc Wilcoxon signed-rank test was used to assess differences in the subjective analyses. Two-tailed $P < .05$ was considered indicative of a statistically significant difference. All statistical analyses were performed in R (version 4.1.1, The R Foundation).

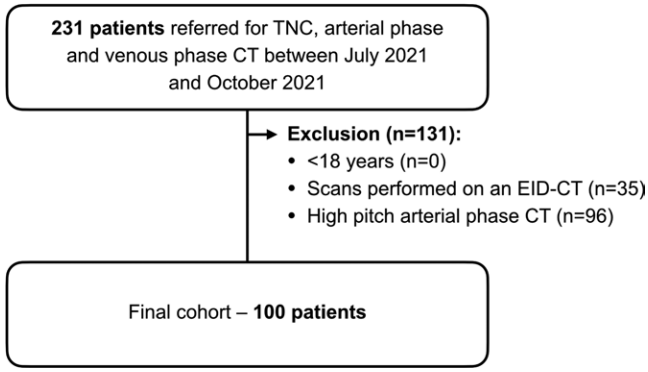

Figure 3: Flowchart shows patient inclusion. EID-CT = energy-integrating detector CT, TNC = true noncontrast.

Table 1: Patient Demographics

Characteristic	Value (*n* = 100)
Sex	
F	19
M	81
Age (y)*	72 ± 10
Body weight (kg)*	79 ± 16
Body mass index (kg/m^2)*	27 ± 4
Indications for imaging	
Follow-up after endovascular aortic repair	70
Follow-up of descending aortic aneurysm	16
Follow-up after acute aortic syndrome	10
Follow-up after open vascular repair	4
Liver lesions	21
Cysts	19
Hemangioma	1
Hepatocellular carcinoma	1
Lesion-to-background contrast (HU)	21
TNC*	40 ± 13
VNC*	35 ± 13
Contrast-to-noise ratio	21
TNC*	3.1 ± 1.4
VNC*	2.4 ± 1.2

Note.—Except where indicated, data are numbers of patients. Lesion-to-background and contrast-to-noise ratios significantly differed between TNC and VNC images ($P = .01$ and $P < .001$, respectively). TNC = true noncontrast, VNC = virtual nonconatrast.
* Data are means ± SDs.

Results

Patient Characteristics

Of 231 patients referred for follow-up examinations of aortic abnormalities, 131 patients were excluded. Of the excluded patients, 35 were examined with EID CT and 96 underwent examinations that included high-pitch arterial phase CT. The remaining 100 consecutive patients (mean age, 72 years ± 10

Table 2: Scan Parameters and Radiation Doses in Patients

Scan Parameters	TNC Scan	Contrast-enhanced Arterial Scan	Contrast-enhanced Portal Venous Scan
Tube voltage (kV)	120	120	120
CARE kV setting	Noncontrast	Vascular	Soft tissue with contrast material
Tube current (mAs)	70 ± 20	49 ± 17	55 ± 17
Radiation doses			
Volume CT dose index (mGy)	5.5 ± 1.6	3.8 ± 1.3	4.4 ± 1.3
Dose-length product (mGy·cm)	378 ± 118	261 ± 95	298 ± 98
Size-specific dose estimate (mGy)	6.6 ± 1.2	4.6 ± 1.2	4.2 ± 1.1

Note.—Except where indicated, data are means ± SDs. TNC = true noncontrast, VNC = virtual noncontrast.

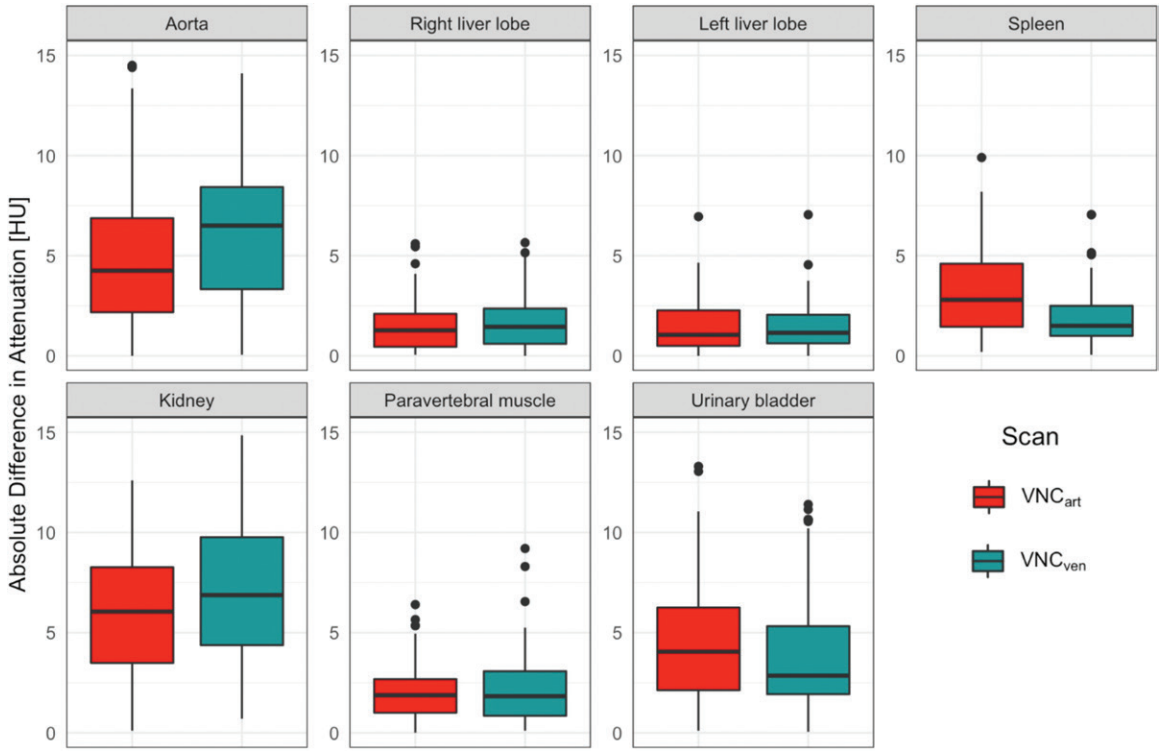

Figure 4: Absolute error of CT attenuation. Boxplots demonstrate the absolute attenuation errors (in Hounsfield units) of arterial virtual noncontrast (VNC$_{art}$) and venous virtual noncontrast (VNC$_{ven}$) images compared with true noncontrast images. Horizontal lines in the boxes indicate the median and the top and bottom lines of boxes indicate the first and third quartiles, respectively. Whiskers show lowest and highest values within 1.5 IQR of the lower and upper limits, and circles indicate outliers.

[SD]; 81 men; mean body mass index, 27 kg/m^2 ± 4) were included in the final sample (Fig 3). Imaging was performed for vascular indications in the majority of patients (Table 1). Hepatic lesions were present in 21 of 100 (21%) patients. Radiation dose parameters for the patients are summarized in Table 2.

Objective Image Quality

Patients.—Interreader agreement of the attenuation errors of the VNC images was substantial (α = .60). Figure 4 depicts the attenuation errors of the VNC images of all evaluated regions. The smallest attenuation errors of the VNC images were found in the left liver lobe for those reconstructed from both arterial and portal venous phase CT (mean, 1.4 HU ± 1.3 and 1.5 HU ± 1.2, respectively) (Table 3).

Attenuation errors of the VNC images from arterial phase CT were less than 5 HU in 99% (99 of 100 patients) for the left liver lobe, 98% (98 of 100 patients) for the right liver lobe, 96% (96 of 100 patients) for the paravertebral muscle, and 80% (80 of 100 patients) for the spleen (Table 4). Attenuation errors of the VNC images from portal venous phase CT were less than 5 HU in 99% (99 of 100 patients) for the left liver lobe, 98% (98 of 100 patients) for the right liver lobe, 95% (95 of 100 patients) for the paravertebral muscle, and 96% (96 of 100 patients) for the spleen. There was no evidence of significant differences between attenuation errors of the VNC images reconstructed from arterial or portal venous phase CT for the left and right liver lobes, paravertebral muscle, and urinary bladder (all, $P > .05$) (Table 3). Attenuation errors of the VNC images reconstructed from arterial phase CT showed smaller errors for the aorta (mean, 5.0 HU ± 3.6 vs 6.1 HU ± 3.4; $P = .04$) and

Table 3: Absolute Error in CT Attenuation between VNC and TNC Images

Region	Arterial VNC Images (HU)	Venous VNC Images (HU)	*P* Value
Aorta	5.0 ± 3.6 (11.3)	6.1 ± 3.4 (13.8)	.04
Right liver lobe	1.5 ± 1.2 (2.5)	1.6 ± 1.3 (2.6)	>.99
Left liver lobe	1.4 ± 1.3 (2.2)	1.5 ± 1.2 (2.4)	>.99
Spleen	3.2 ± 2.2 (6.0)	1.9 ± 1.4 (3.6)	<.001
Kidney	6.0 ± 3.3 (16.3)	7.2 ± 3.4 (19.6)	<.001
Paravertebral muscle	2.0 ± 1.4 (4.2)	2.2 ± 1.7 (4.6)	>.99
Urinary bladder	4.4 ± 3.0 (27.5)	3.9 ± 2.9 (24.4)	.10

Note.—Except where indicated, data are means ± SDs, with the percentage error relative to the mean attenuation determined from TNC images in parentheses. TNC = true noncontrast, VNC = virtual noncontrast.

Table 4: Absolute Error in CT Attenuation Less than 5 HU and 10 HU

Region	Arterial VNC Images		Venous VNC Images	
	<5 HU	<10 HU	<5 HU	<10 HU
Aorta	58	91	41	87
Right liver lobe	98	100	98	100
Left liver lobe	99	100	99	100
Spleen	80	100	96	100
Kidney	37	87	28	76
Paravertebral muscle	96	100	95	100
Urinary bladder*	63	97	72	93
Total	76	96	76	94

Note.—Data are percentages of patients (n = 100) with a CT attenuation difference between true noncontrast and virtual noncontrast (VNC) images less than 5 HU and 10 HU, respectively. Region of interest–based measurements were averaged between two readers.

* The urinary bladder was empty in 13 of 100 patients.

kidney (mean, 6.0 HU ± 3.3 vs 7.2 HU ± 3.4; $P < .001$) compared with VNC images reconstructed from portal venous phase CT. For the spleen, attenuation errors of the VNC images reconstructed from portal venous phase CT were smaller compared with those reconstructed from arterial phase CT (mean, 1.9 HU ± 1.4 vs 3.2 HU ± 2.2; $P < .001$). Table E1 (online) shows the mean CT attenuation of all assessed regions.

***Phantom.*—**Results of the noise (NPS) and spatial resolution (TTF) analyses are summarized in Figure 5. NPS curves depicted a higher image noise amplitude at low spatial frequencies (<0.1 mm^{-1}) for VNC compared with TNC images. Average spatial frequency shifted toward lower frequencies, from 0.2 mm^{-1} for TNC to 0.14 mm^{-1} for VNC, indicating blotchier noise texture. The square root of the area under the NPS curve, representing noise magnitude, was 33% higher in VNC than in TNC images. The TTF was 0 at 1.0 mm^{-1} for both reconstructions. The TTF of TNC images was higher at high frequencies compared with the TTF of VNC images (TTF at 90% of its maximum value was equal to 0.08 mm^{-1} and 0.06 mm^{-1} for TNC and VNC, respectively), although this tendency was reversed at low frequencies (TTF at 10% of its maximum value [TTF_{10}] was equal to 0.59 mm^{-1} and 0.69 mm^{-1} for TNC and VNC, respectively, corresponding to a 17% higher TTF_{10} in VNC than TNC images). TTF achieved identical values at the middle frequency range (TTF at 50% of its maximum value was equal to 0.29 mm^{-1} in both cases). The detectability index of VNC images had an average reduction of 15% compared with TNC images but was always higher than 20.

Subjective Image Quality

Figure 6 provides an overview of the subjective results. Interreader agreement was moderate for image quality, subjective image noise, noise texture, and delineation of small structures (α = .50, .52, .54, and .45, respectively). No artifacts were found on any of the VNC images reconstructed from arterial or portal venous phase CT. For both readers, scores of TNC images were rated higher compared with VNC images reconstructed from arterial and portal venous phase CT for all categories (all, $P < .001$) (Tables E2, E3 [online]). Image quality and subjective image noise were similar between VNC images reconstructed from arterial and portal venous phase CT (all, $P > .05$) (Table E3 [online]). The noise texture of VNC images reconstructed from portal venous phase CT was rated superior to that of VNC images reconstructed from arterial phase CT by one reader ($P = .60$ for reader 1 and $P = .046$ for reader 2). Regarding the delineation of small structures, VNC images reconstructed from portal venous phase CT achieved superior scores compared with those reconstructed from arterial phase CT ($P = .04$ for reader 1 and $P < .001$ for reader 2). Overall, the percentage of images with diagnostic image quality was very high for all three reconstructions (TNC, 100% and 100%; VNC images reconstructed from arterial phase CT, 99% and 100%; and VNC images reconstructed from portal venous phase CT, 99% and 100% for readers 1 and 2, respectively).

Discussion

Inherent spectral capabilities of photon-counting detector (PCD) CT allow for the reconstruction of virtual noncontrast (VNC) images from contrast-enhanced scans. To replace true noncontrast (TNC) scans, accurate CT attenuation values and diagnostic quality of VNC images are mandatory. In this phantom and patient study, we investigated CT attenuation error, objective image quality, and subjective image quality of VNC images from arterial and portal venous phase scans acquired with a first-generation, clinical, dual-source PCD CT scanner. In patients, our results indicate a low absolute error of CT attenuation of VNC images in various abdominal organs and regions. Overall, attenuation errors of VNC images were less than 5 HU in 76% and less than 10 HU in 95% of measurements compared with TNC images. Subjective analysis of image quality revealed inferior overall image quality and delineation of small structures, higher image noise, and blotchier image noise texture

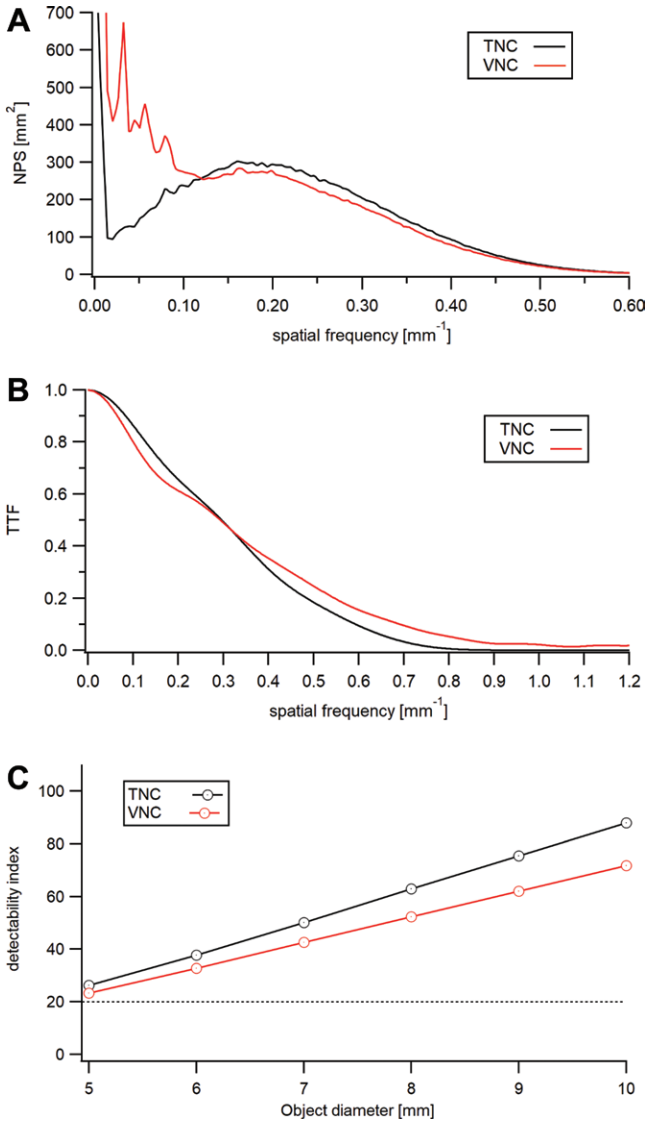

Figure 5: Noise power spectrum (NPS), task transfer function (TTF), and detectability index in the phantom. **(A)** Graph shows NPS curves for true noncontrast (TNC) and virtual noncontrast (VNC) images averaged across the three phantom scans. The higher image noise amplitude at low spatial frequencies for VNC compared with TNC images indicates blotchier noise texture. **(B)** Graph shows TTF curves for TNC and VNC images averaged across the three phantom scans. TTF was comparable at the middle frequency range, highlighting the similar spatial resolution between TNC and VNC images. **(C)** Graph shows the detectability index for TNC and VNC images averaged across the three phantom scans. The detectability index was adjusted to take into account the lesion contrast of hepatic lesions in patients and was always higher than 20, indicating high diagnostic accuracy.

of VNC compared with TNC images (all, $P < .001$). However, the overall image quality of VNC images was rated diagnostic in 99%–100% of patients. The phantom study revealed 33% higher image noise and blotchier image noise texture of VNC compared with TNC images, while spatial resolution remained similar (identical task transfer function [TTF at 50% of its maximum value]). The detectability index of VNC showed high diagnostic accuracy (detectability index >20), although 15% inferior compared with TNC.

Several former studies have shown inaccurate CT attenuation in VNC images derived from EID CT (7,10,11,30). Sauter et al (30) evaluated VNC images of the abdomen in 63 patients and found differences of 10 HU or more between TNC and VNC images in nearly 20% of all measurements. Ananthakrishnan et al (31) compared attenuation values of VNC with TNC images in 46 patients and reported attenuation differences of less than 5 HU in only 44% of the measurements. Our results indicate attenuation differences of less than 5 HU in a notable 76% of measurements, yielding improved attenuation accuracy of VNC images acquired with PCD CT compared with EID CT. These findings are in accordance with results of a recent comparative phantom study evaluating the attenuation error of VNC images of the liver reconstructed from the same PCD CT scanner used in the current study and a third-generation, dual-source, dual-energy EID CT scanner (32). Attenuation errors were significantly lower for VNC images acquired with PCD CT compared with EID CT ($P < .001$). The attenuation errors of the liver parenchyma (mean, 1.5 HU ± 1.8) were comparable with those found in VNC images in our study (mean, 1.4 HU ± 1.3 and 1.5 HU ± 1.2 for the left liver lobe).

The phantom part of our study showed higher image noise and lower noise frequency content of VNC compared with TNC images, indicating blotchier image noise texture. A similar shift to lower noise frequencies has been described as a typical finding for iterative reconstruction algorithms (33–35). Spatial resolution, represented by the task transfer function, indicated similar results for TNC and VNC images. As described by Rajagopal et al (28), the detectability index was used as a measure of objective image quality. In the literature, a detectability index greater than or equal to 5 corresponds to high accuracy and diagnostic image quality (27). In our study, although inferior to TNC, the detectability index of VNC was always higher than 20, indicating high diagnostic accuracy.

Findings of our phantom study matched the observations of the subjective image quality assessment in patients. We found inferior subjective image quality of VNC compared with TNC images. This is in line with the findings of Lehti et al (36), who reported higher subjective image quality of TNC compared with VNC images acquired with EID CT. Overall, in our study, the subjective image quality, image noise, and noise texture of VNC images reconstructed from arterial and portal venous phase CT were still rated as "good" by both readers. Apart from delineation of small structures, for which both readers preferred VNC images reconstructed from portal venous phase CT, and noise texture, for which one reader preferred VNC images reconstructed from portal venous phase CT, no evidence of significant differences was found between VNC images reconstructed from arterial and portal venous phase CT.

It is important to note that postprocessing algorithms in PCD CT must be tailored to the diagnostic task. With the clinical release of PCD CT, the vendor implemented two different VNC algorithms; the first is a conventional VNC algorithm, which was evaluated in our study and which is tailored to measure CT attenuation in parenchymal structures, and the second is an algorithm tailored to vascular and stent imaging (Pure Calcium; Siemens Healthcare). The VNC algorithm evaluated in our study is used to subtract iodine-based contrast material from parenchymatous organs and improve quantitative attenuation

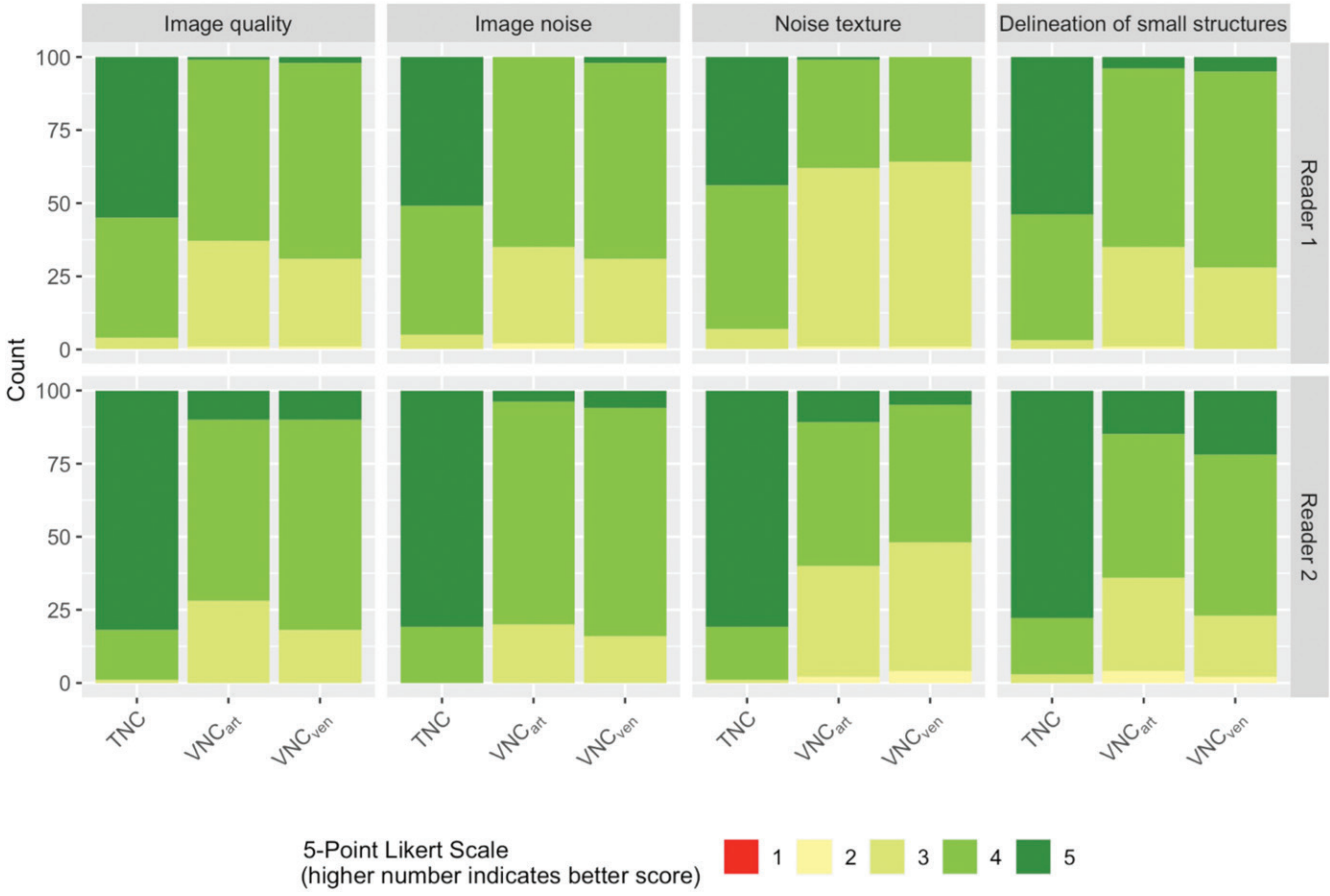

Figure 6: Subjective image quality. Bar graphs show qualitative scores for image quality, image noise, noise texture, and delineation of small structures as scored by two independent readers using a five-point discrete visual scale. True noncontrast (TNC) images outperformed virtual noncontrast reconstructions in all categories assessed, while arterial virtual noncontrast (VNC_{art}) and venous virtual noncontrast (VNC_{ven}) images were still rated good by both readers.

measurements (eg, lesion characterization). However, known shortcomings of this algorithm are altered visualization and possible erroneous subtraction of calcified structures such as vascular calcifications or high attenuating material, including stents (37). When the aim is to visualize calcifications or metallic structures after subtracting iodine, the second virtual noncontrast postprocessing algorithm should be used (37,38).

The following study limitations merit consideration. First, subjective analysis of image noise in patients was likely influenced by small differences in the radiation dose between TNC and contrast-enhanced scans. This was due to the CARE kV algorithm, which resulted in a lower radiation dose for the contrast-enhanced scans. Nevertheless, this scan protocol represents the clinically recommended and meaningful protocol, as the different phases were optimized for the intended clinical task (eg, optimization for noncontrast in TNC imaging and optimization for contrast-enhanced imaging in arterial and portal venous phase scans). To mitigate this limitation, we also performed objective image quality analysis in the phantom at matched radiation doses. Second, we did not investigate the impact of VNC images on lesion characterization or detection. Instead, we used the detectability index as a surrogate for overall diagnostic image quality. Finally, we did not compare the accuracy of VNC images acquired with a PCD CT scanner with that of other CT scanners with other dual-energy approaches.

In conclusion, virtual noncontrast (VNC) images acquired with photon-counting detector (PCD) CT demonstrated high accuracy of CT attenuation in the abdomen with inferior but overall good objective and subjective image quality compared with true noncontrast (TNC) images. Because PCD CT inherently offers the possibility of VNC reconstruction and the radiation dose can be reduced by omitting a TNC scan, VNC imaging has the potential to become the new clinical standard in the near future. Further studies should focus on the value of VNC images for lesion characterization.

Acknowledgment: We thank Mrs Sarah Euler, MSCN, for revising the manuscript.

Author contributions: Guarantors of integrity of entire study, **V.M., L.J., H.A., A.E.**; study concepts/study design or data acquisition or data analysis/interpretation, all authors; manuscript drafting or manuscript revision for important intellectual content, all authors; approval of final version of submitted manuscript, all authors; agrees to ensure any questions related to the work are appropriately resolved, all authors; literature research, **V.M., D.R., L.J., K.H., H.A., A.E.**; clinical studies, **V.M., L.J., S.B., K.H., K.M., H.A., A.E.**; experimental studies, **D.R., P.M.**; statistical analysis, **V.M., D.R., T.S., H.A.**; and manuscript editing, **V.M., D.R., T.S., S.B., K.H., K.M., H.A., A.E.**

Data sharing: Data generated or analyzed during the study are available from the corresponding author by request.

Disclosures of conflicts of interest: V.M. No relevant relationships. **D.R.** No relevant relationships. **L.J.** No relevant relationships. **T.S.** No relevant relationships. **S.B.** No relevant relationships. **P.M.** No relevant relationships. **K.H.** No relevant relationships. **K.M.** No relevant relationships. **H.A.** No relevant relationships. **A.E.** No relevant relationships.

References

1. Mileto A, Ananthakrishnan L, Morgan DE, Yeh BM, Marin D, Kambadakone AR. Clinical Implementation of Dual-Energy CT for Gastrointestinal Imaging. AJR Am J Roentgenol 2021;217(3):651–663.
2. Sun H, Hou XY, Xue HD, et al. Dual-source dual-energy CT angiography with virtual non-enhanced images and iodine map for active gastrointestinal bleeding: image quality, radiation dose and diagnostic performance. Eur J Radiol 2015;84(5):884–891.
3. Haji-Momenian S, Parkinson W, Khati N, Brindle K, Earls J, Zeman RK. Single-energy non-contrast hepatic steatosis criteria applied to virtual non-contrast images: is it still highly specific and positively predictive? Clin Radiol 2018;73(6):594.e7–594.e15.
4. Gnannt R, Fischer M, Goetti R, Karlo C, Leschka S, Alkadhi H. Dual-energy CT for characterization of the incidental adrenal mass: preliminary observations. AJR Am J Roentgenol 2012;198(1):138–144.
5. Nagayama Y, Inoue T, Oda S, et al. Adrenal Adenomas versus Metastases: Diagnostic Performance of Dual-Energy Spectral CT Virtual Noncontrast Imaging and Iodine Maps. Radiology 2020;296(2):324–332.
6. Graser A, Johnson TR, Hecht EM, et al. Dual-energy CT in patients suspected of having renal masses: can virtual nonenhanced images replace true nonenhanced images? Radiology 2009;252(2):433–440.
7. Meyer M, Nelson RC, Vernuccio F, et al. Virtual Unenhanced Images at Dual-Energy CT: Influence on Renal Lesion Characterization. Radiology 2019;291(2):381–390.
8. Xiao JM, Hippe DS, Zecevic M, et al. Virtual Unenhanced Dual-Energy CT Images Obtained with a Multimaterial Decomposition Algorithm: Diagnostic Value for Renal Mass and Urinary Stone Evaluation. Radiology 2021;298(3):611–619.
9. Ma G, Han D, Dang S, et al. Replacing true unenhanced imaging in renal carcinoma with virtual unenhanced images in dual-energy spectral CT: a feasibility study. Clin Radiol 2021;76(1):81.e21–81.e27.
10. Cao J, Lennartz S, Pisuchpen N, Parakh A, Kambadakone A. Attenuation values on virtual unenhanced images obtained with detector-based dual-energy computed tomography: observations on single- and split-bolus contrast protocols. Abdom Radiol (NY) 2021. 10.1007/s00261-021-03273-8. Published online October 23, 2021.
11. Borhani AA, Kulzer M, Iranpour N, et al. Comparison of true unenhanced and virtual unenhanced (VUE) attenuation values in abdominopelvic single-source rapid kilovoltage-switching spectral CT. Abdom Radiol (NY) 2017;42(3):710–717.
12. Durieux P, Gevenois PA, Muylem AV, Howarth N, Keyzer C. Abdominal Attenuation Values on Virtual and True Unenhanced Images Obtained With Third-Generation Dual-Source Dual-Energy CT. AJR Am J Roentgenol 2018;210(5):1042–1058.
13. Rajendran K, Petersilka M, Henning A, et al. First Clinical Photon-counting Detector CT System: Technical Evaluation. Radiology 2022;303(1):130–138.
14. Symons R, De Bruecker Y, Roosen J, et al. Quarter-millimeter spectral coronary stent imaging with photon-counting CT: Initial experience. J Cardiovasc Comput Tomogr 2018;12(6):509–515.
15. Symons R, Pourmorteza A, Sandfort V, et al. Feasibility of Dose-reduced Chest CT with Photon-counting Detectors: Initial Results in Humans. Radiology 2017;285(3):980–989.
16. Higashigaito K, Euler A, Eberhard M, Flohr TG, Schmidt B, Alkadhi H. Contrast-Enhanced Abdominal CT with Clinical Photon-Counting Detector CT: Assessment of Image Quality and Comparison with Energy-Integrating Detector CT. Acad Radiol 2022;29(5):689–697.
17. Si-Mohamed SA, Sigovan M, Hsu JC, et al. In Vivo Molecular K-Edge Imaging of Atherosclerotic Plaque Using Photon-counting CT. Radiology 2021;300(1):98–107.
18. Nowak T, Eberhard M, Schmidt B, et al. Bone Mineral Density Quantification from Localizer Radiographs: Accuracy and Precision of Energy-integrating Detector CT and Photon-counting Detector CT. Radiology 2021;298(1):147–152.
19. Euler A, Higashigaito K, Mergen V, et al. High-Pitch Photon-Counting Detector Computed Tomography Angiography of the Aorta: Intraindividual Comparison to Energy-Integrating Detector Computed Tomography at Equal Radiation Dose. Invest Radiol 2022;57(2):115–121.
20. Zhou W, Michalak GJ, Weaver JM, et al. A Universal Protocol for Abdominal CT Examinations Performed on a Photon-Counting Detector CT System: A Feasibility Study. Invest Radiol 2020;55(4):226–232.
21. Leng S, Rajendran K, Gong H, et al. 150-μm spatial resolution using photon-counting detector computed tomography technology: technical performance and first patient images. Invest Radiol 2018;53(11):655–662.
22. Muenzel D, Bar-Ness D, Roessl E, et al. Spectral Photon-counting CT: Initial Experience with Dual-Contrast Agent K-Edge Colonography. Radiology 2017;283(3):723–728.
23. Pourmorteza A, Symons R, Henning A, Ulzheimer S, Bluemke DA. Dose Efficiency of Quarter-Millimeter Photon-Counting Computed Tomography: First-in-Human Results. Invest Radiol 2018;53(6):365–372.
24. Sartoretti T, Eberhard M, Rüschoff JH, et al. Photon-counting CT with tungsten as contrast medium: Experimental evidence of vessel lumen and plaque visualization. Atherosclerosis 2020;310:11–16.
25. Willemink MJ, Persson M, Pourmorteza A, Pelc NJ, Fleischmann D. Photon-counting CT: technical principles and clinical prospects. Radiology 2018;289(2):293–312.
26. Symons R, Krauss B, Sahbaee P, et al. Photon-counting CT for simultaneous imaging of multiple contrast agents in the abdomen: An in vivo study. Med Phys 2017;44(10):5120–5127.
27. Racine D, Becce F, Viry A, et al. Task-based characterization of a deep learning image reconstruction and comparison with filtered back-projection and a partial model-based iterative reconstruction in abdominal CT: A phantom study. Phys Med 2020;76:28–37.
28. Rajagopal JR, Farhadi F, Solomon J, et al. Comparison of Low Dose Performance of Photon-Counting and Energy Integrating CT. Acad Radiol 2021;28(12):1754–1760.
29. Singh S, Kalra MK, Hsieh J, et al. Abdominal CT: comparison of adaptive statistical iterative and filtered back projection reconstruction techniques. Radiology 2010;257(2):373–383.
30. Sauter AP, Muenzel D, Dangelmaier J, et al. Dual-layer spectral computed tomography: Virtual non-contrast in comparison to true non-contrast images. Eur J Radiol 2018;104:108–114.
31. Ananthakrishnan L, Rajiah P, Ahn R, et al. Spectral detector CT-derived virtual non-contrast images: comparison of attenuation values with unenhanced CT. Abdom Radiol (NY) 2017;42(3):702–709.
32. Sartoretti T, Mergen V, Higashigaito K, Eberhard M, Alkadhi H, Euler A. Virtual Noncontrast Imaging of the Liver Using Photon-Counting Detector Computed Tomography: A Systematic Phantom and Patient Study. Invest Radiol 2022. 10.1097/RLI.0000000000000860. Published online February 7, 2022.
33. Singh R, Digumarthy SR, Muse VV, et al. Image Quality and Lesion Detection on Deep Learning Reconstruction and Iterative Reconstruction of Submillisievert Chest and Abdominal CT. AJR Am J Roentgenol 2020;214(3):566–573.
34. Mileto A, Guimaraes LS, McCollough CH, Fletcher JG, Yu L. State of the Art in Abdominal CT: The Limits of Iterative Reconstruction Algorithms. Radiology 2019;293(3):491–503.
35. Rotzinger DC, Racine D, Beigelman-Aubry C, et al. Task-Based Model Observer Assessment of A Partial Model-Based Iterative Reconstruction Algorithm in Thoracic Oncologic Multidetector CT. Sci Rep 2018;8(1):17734.
36. Lehti L, Söderberg M, Höglund P, Wassélius J. Comparing Arterial- and Venous-Phase Acquisition for Optimization of Virtual Noncontrast Images From Dual-Energy Computed Tomography Angiography. J Comput Assist Tomogr 2019;43(5):770–774.
37. Decker JA, Bette S, Scheurig-Muenkler C, et al. Virtual Non-Contrast Reconstructions of Photon-Counting Detector CT Angiography Datasets as Substitutes for True Non-Contrast Acquisitions in Patients after EVAR-Performance of a Novel Calcium-Preserving Reconstruction Algorithm. Diagnostics (Basel) 2022;12(3):558.
38. Allmendinger T, Nowak T, Flohr T, et al. Photon-Counting Detector CT-Based Vascular Calcium Removal Algorithm: Assessment Using a Cardiac Motion Phantom. Invest Radiol 2022. 10.1097/RLI.0000000000000853. Published online January 11, 2022.